# Elucidating the contact mechanics of aluminum silicon surfaces with Green's function molecular dynamics

Carlos Campañá, Martin H. Müser*, and Colin Denniston†
*Department of Applied Mathematics, University of Western Ontario, London, Ontario N6A 5B7, Canada*

Yue Qi‡ and Thomas A. Perry
*Materials and Processes Laboratory, General Motors R&D Center, Warren, MI 48090-9055*
(Dated: September 13, 2007)

We study the contact mechanics of a flat, elastic wall pressed against a rigid substrate with Green's function molecular dynamics. The substrate's height profiles are parameterized from atomic force microscope topography measurements of two different aluminum-silicon alloys. In both samples, roughness lives on disparate length scales, i.e., on relatively large scales defined by size and mean separation of load-bearing silicon particles and on much smaller scales associated with the roughness on top of individual particles. The major differences between the two alloys are their silicon content and the typical silicon particle geometry. These differences lead to quite different stress distribution on both mesoscale and microscale in our calculations. A common feature is that the stress distribution decays exponentially for large stresses $\sigma$ and not like a Gaussian. Persson's contact mechanics theory is generalized to the case where contact can only occur on silicon particles. This generalization predicts relatively accurate microscopic mean square stresses, however it fails to predict accurate numbers for mean square stresses on the mesoscopic scales. Local overlap models are not accurate either, because they fail to describe the contact morphology.

PACS numbers: 81.40.Pq,46.55.+d

## I. INTRODUCTION

Making liner-less engine blocks cast directly from lightweight Al-Si alloys with the required wear and scuffing properties continues to be a challenge for the automotive industry. [1] Aluminum is typically protected by an inert oxide layer, however this layer can be damaged under higher loads and the strong adhesion tendency of nascent aluminum to the counter surfaces will accelerate the damage into a scuffing process. An approach to mitigating this is to include a hard reinforcement in the alloy, such as silicon. This is very effective under lubricated operating conditions. Liner-less engine blocks made of a hypereutectic Al-Si alloy typically require a chemical surface preparation that results in silicon particles protruding above the nominal surface to reduce wear damage to the aluminum matrix. [2, 3] Thus, these hard silicon particles (hardness $\approx$ 12 GPa) will bear the load, prevent adhesion, and resist wear damage. [4]

The wear mechanisms of Al-Si alloys under dry sliding have been reviewed by Deuis et al. [5] Depending on the applied load, three wear regimes have been proposed: [6]1) mild wear: wear rates of $10^{-4}$ to $10^{-3}$ mm$^3$/m under low load; 2) severe wear: wear rates of order $10^{-2}$ mm$^3$/m, often under dry sliding conditions; 3) seizure wear: extensive material transfer occurs at high temperature and high load. Recently, an ultra-mild wear regime, where a negligible amount of material is removed per cycle, gained more attention. Cylinder bores made of Al-Si alloys are expected to be in this regime if they are operated under normal engine running conditions. [7]The contact pressure on Al-Si surface is therefore crucial in determining the deformation and failure of Al-Si in the tribological applications.

To improve the wear and scuffing resistance of Al-Si alloys, many metallurgy design methods, such as heat treatment, alloying additions, and increasing the silicon content have been tried to strengthen Al-Si alloys. However, the origin of improved tribological performance is not always clear, because the complexity of the surface topography makes it difficult to predict their contact mechanics. Therefore the motivation of this paper is to understand the load distribution as a function of silicon particle shape and to provide metallurgical guidance for alloy development. With such a connection between contact pressure and microstructure, one can improve Al-Si alloy composition and processing to enhance the wear resistance, and ultimately to develop a linerless aluminum cylinder block for the automotive lightweight strategy.

Being able to predict the distribution of loads on the silicon particles and more generally, being able to predict the pressure distribution in contacts involving an Al-Si

*mmuser@uwo.ca; http://publish.uwo.ca/ mmuser/; Financial support from the Natural Sciences and Engineering Research Council of Canada and the Ontario Ministry of Energy is gratefully acknowledged as well as access to high-performance computing through Sharcnet.
†cdennist@uwo.ca; Financial support from the Natural Sciences and Engineering Research Council of Canada and access to high-performance computing through Sharcnet is greatfully acknowledged.
‡yue.qi@gm.com; YQ would like to thank Shuman Xian for preparing the samples, Dr. Carl Fuerst for the help on setting up the collaboration, and Dr. A. K. Sachdev, Y. T. Cheng, K. S. Kim, S. Biswas, and Alpas for stimulating discussions.

surface and a flat counter surface bears potential for an improved design of the surfaces. As a step towards a better understanding of their contact mechanics, we consider the case of dry contacts. Experimentally-measured height profiles will be used as an input for a theoretical analysis that is based on a recently developed Green's function molecular dynamics (GFMD) formalism. [8]

The difficulty in the contact mechanics of Al-Si alloys stems from their complex geometry. Their surfaces are not self-affine like those of conventional steel surfaces. Instead they have roughness on disparate length scales as demonstrated in figures 1 and 2. On large length scales there is roughness due to the granular structure, i.e., the typical height and diameter of the silicon particles are 300 nm and $4-10$ $\mu$m, respectively. The spacing in between the particles is typically in the order of 4 $\mu$m. At short length scales there remains some roughness on the silicon particles that is due to polishing.

Theoretical models, whether they are phenomenological, such as Greenwood-Williamson (GW) [9] or based on height-difference autocorrelation functions, such as Persson's theory cannot be used to address the contact mechanics of Al-Si surfaces in a straightforward fashion even in the limit of elastic contacts. For instance, GW approaches are inappropriate to apply, [7, 10] because they assume that local surface roughness is parabolic, which is unjustified in the present context. Even if more realistic shapes were assumed, the lack of long-range elastic deformation in GW will limit the predictive power of this theory. Conversely, Persson's theory appears to be generalizable to the case where contact only occurs on the silicon particles, as we will outline in the main part of this paper.

We wish to comment that throughout this paper, the word pressure will refer to the external load exerted per unit area onto the elastic solid. The term stress will refer to the $\sigma_{33}$ component of the elastic solid's full stress tensor. With these definitions, we will use the terms stress and pressure as synonyms in static equilibrium. Moreover, we will assume that the small-slope approximation holds in the contact region. Thus, we will usually not distinguish between the local surface normal and the average surface normal.

The remainder of the paper is organized as follows: In Sec. II, we provide experimental details on chemical composition and treatment of the surfaces along with the numerical methodology used to solve the harmonic contact problem. A brief description of Persson's contact mechanics theory, as well as our extension to surfaces with granular structure is presented in Sec. III. Results are presented in Sec. IV and conclusions are drawn in Sec. V.

## II. EXPERIMENTAL DETAILS, MODEL AND METHOD

### A. Experimental detail

Two different types of Al-Si alloys are investigated in this study. Typical topographies are shown in Fig. 1. In part (a) of that figure, the tops of the silicon-rich particles are almost circular while in part (b), they are much more elongated. In the following, we will refer to the samples as surfaces with circular or elongated silicon particles, respectively. Surfaces with circular particles (material A1955) stem from a hypoeutectic A356 aluminum alloy containing 7 wt.% Si and 0.3 wt.% Mg and 0.05 wt.% Sr. Surfaces with elongated silicon particles (material A1934) are based on a near-eutectic Al-Si alloy with 11.3 wt.% Si and other alloying components, specifically Cu, Mn, Fe, Ti, Mg, Sr, Ni, and Zn.

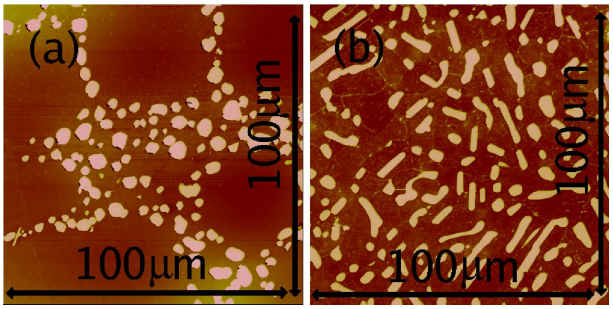


FIG. 1: Online color. Topographies of samples containing predominantly (a) circular and (b) elongated silicon particles. Light sections are silicon-rich particles, dark sections primarily aluminum. In both cases, the full 100 $\mu$m $\times$ 100 $\mu$m scan is shown.

Each specimen was cut from an Al/Si cast ingot into a plate shape with dimensions of 12mm $\times$ 12mm $\times$ 3mm using a diamond saw. The contact surface was ground with SiC paper of 320 and 500 grit, followed by mechanical polishing with 9 $\mu$m, 6 $\mu$m, and 3 $\mu$m diamond suspensions. A final stage of chemical-mechanical polishing with colloidal silica was performed to obtain a fine surface finish and reduce the surface deformation layer created in the previous mechanical polishing steps. To expose the silicon particles on the sample surface, the specimen was chemically etched with 10% NaOH solution for 45 seconds, and then cleaned with 2% HNO for 20 seconds. The average exposed height of the silicon particles was measured by an atomic force microscope (AFM) to be about 350 nm, which was less than 1/10 of the average particle size. Therefore most of the particles on the surface were still deeply embedded in the aluminum matrix.

Both alloys show silicon particles embedded in the aluminum matrix. Height profiles were measured with the help of an atomic force microscope tip. Measurement points are separated by 30 nm. The statistical analysis shows that the silicon particle linear size varies from 2 to 15 $\mu$m with an aspect ratio between 1 and 6 in ("circu-

lar") A1955 and from 3 to 20 $\mu$m with the aspect ratio between 1 and 10 in ("elongated") A1934. Details of selected individual silicon particles are shown in Fig. 2. In those silicon particles, the aspect ratios are 1.1 and 5.2 for A1955 and A1934, respectively. Further characterization of the samples will be presented in the results section.

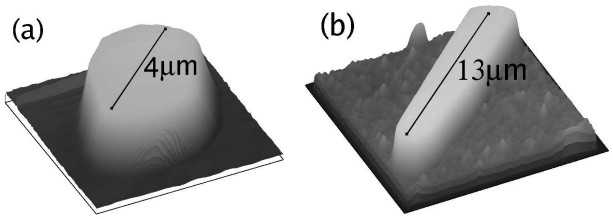


FIG. 2: Details of (a) circular and (b) elongated silicon particles embedded in an aluminum matrix. Note that the direction normal to the surface is exaggerated with respect to the in-plane directions. The height of the asperities is approximately 300 $nm$.

### B. Model

As mentioned in the introduction, we study a flat elastic manifold that is pressed against a rough wall, whose height profile is input from experiment. In our calculations, we mean to exploit the usual mapping for frictionless contacts, whereby all the roughness can be placed on one side of the interface while all the elasticity is placed on the other side.

Our main interest is to model an Al-Si alloy that is pressed against a chromium counterface, which can be approximated as locally flat. Since the chromium counterpart is much stiffer and less rough than the Al-Si alloy, we assume that both the effective modulus and the roughness to be used in the calculation is mainly determined by the values in the Al-Si alloy. At a first level of approximation, the Young's modulus of the Al-Si is calculated with the combination rule $E_{\rm alloy} = E_{\rm Si}c_{\rm Si} + E_{\rm Al}c_{\rm Al}$, where the moduli $E$ are weighted by the volumetric weights ($c_{\rm Si}$ and $c_{\rm Al}$) of the two compounds. Assuming $E_{\rm Si} = 160$ GPa and $E_{\rm Al} = 70$ GPa, for the moduli, we obtain almost identical values for the two alloys, specifically, $E = 76$ and $E = 81$ GPa for the samples with circular and elongated silicon particles, respectively.

Excluded volume interactions are assumed between the flat, elastically-deformable surface and the rough, rigid surface. Plastic deformation is neglected at this stage of our work. Whenever the normal stress is high, we would expect the surfaces to yield locally but not to rearrange so strongly that it would significantly affect the load carried by adjacent silicon particles.

### C. Method

All calculations presented in this work are based on the Green's function molecular dynamics (GFMD) method that was recently developed by Campañá and Müser. [8] In GFMD, the three-dimensional elastic solid is mapped onto a two-dimensional elastic sheet with long-range elastic interactions. Computation of the elastic interaction within the sheet is relatively inexpensive in reciprocal space, at least as long as the solid can be approximated as harmonic and homogeneous. For the system sizes considered in this work, i.e., linear dimension of 2048 grid points, the computational gain of GFMD per time step with respect to an all-atom calculation (which would require about 2048 layers in the direction normal to the surface) is in the order of 268 (=2048/ln2048). Approaches in which the system is ever more coarse grained as the distance from the surfaces increases show a linear gain in efficiency with increasing the linear dimension per time step. However, GFMD appears to approach mechanical equilibrium particularly fast and may thus require fewer steps to converge than approaches that are based on coarse-graining entirely in real space. It certainly requires a lot fewer time steps to equilibrate than an all-atom calculations, as demonstrated in our previous work. [8]

Periodic boundary conditions are applied to facilitate the use of the Green's function methodology. To reduce artifacts and discontinuities near the boundaries, the height profiles are folded with a function that is unity everywhere, except near the boundaries, where it continuously approaches zero.

As the substrate is rough, the pressure at the interface between the substrate and the opposing surface is non-uniform. Pressures and their histograms were calculated and averaged at different levels of magnification - or coarse-grainedness, that is, at a macroscopic, a mesoscopic, and a microscopic level. The macroscopic pressure is given by the external load $L$ divided by the area of the scan $A_0$. The macroscopic pressure distribution $P_{\rm macro}(p)$ is automatically a $\delta$ function, i.e.,

$$P_{\rm macro}(p) = \delta(p - L/A_0) \tag{1}$$

The mesoscopic pressure associated with asperity $i$ is calculated as the load $F_i$ that $i$ carries divided by its surface area, $A_i$. To place a larger statistical weight on larger silicon particles, the pressure $p_i$ is assigned a stochastic weight proportional to the silicon particle's area, i.e., the meso-scale pressure distribution is defined as:

$$P_{\rm meso}(p) = \frac{\sum_i A_i \delta(p - p_i)}{\int_{0^+}^{\infty} dp \sum_i A_i \delta(p - p_i)}, \tag{2}$$

where the normalization in the denominator of Eq. (2) includes only the load-bearing particles. Asperities were enumerated with the help of the Hoshen-Kopelman algorithm. [11]

Finally, the microscopic pressure, $p_{\rm micro}$ is the value that one obtains locally when the discretization of the elastic manifold is much finer than the shortest wavelength $\lambda_{\rm s}$ on which roughness is found on the surface profile. The microscopic pressure distribution is given by a similar expression as that in Eq. (2), however, now $i$ does not denote a silicon particle but an integration grid point. In this work, $\lambda_{\rm s}$ is given by the typical size of the final powder that was used to polish the surface, i.e., $\lambda_{\rm s} \approx 50$ nm. The experimental resolution of the height scans is a little higher, that is $\lambda_{\rm resol} = 30$nm, but there is not significant roughness associated at scales below $\lambda_{\rm resol}$.

One can summarize the meaning of macroscopic, mesoscale, and microscopic pressure as follows: The macroscopic pressure is the total load divided by the total area. Mesoscopic pressures are microscopic pressures averaged over an area associated with a typical particle area, or simply, the load carried by an individual particle divided by its area. Microscopic pressures or stresses are defined as $\lim_{\Delta A \to 0} \Delta L/\Delta A$, where $\Delta L$ is the load carried by an infinitesimally small area element $\Delta A$.

## III. THEORY

### A. Background

In this work, we will compare our numerically obtained data to Persson's contact mechanics theory [12–14] whenever a comparison appears appropriate. In order to facilitate our extension to the structure of Al-Si alloys, we use the opportunity to sketch a derivation of the theory, which roughly follows the original treatment. In our presentation, we will attempt to distinguish between those steps that are rigorous and those that are approximations.

The key idea of Persson's theory is to gradually increase the magnification $\zeta$ at which the system is described. At magnification $\zeta = 1$, the system is described at the most coarse-grained level, i.e., at the length scale of the macroscopic object $\mathcal{L}$. At this level of magnification, the pressure distribution is a delta function centered at the macroscopic pressure, i.e., $P(\sigma, \zeta = 1) = \delta(\sigma - \sigma_0)$. As $\zeta$ increases, spatial features are resolved. In the limit $\zeta \to \infty$, all microscopic details of the system are fully contained. We will call $P(\sigma) = \lim_{\zeta \to \infty} P(\sigma, \zeta)$ a microscopic pressure distribution.

The starting point of the theory is the definition of the coarse-grained local pressure at magnification $\zeta$, i.e., $\sigma(\mathbf{x}, \zeta)$. The definition of $\sigma(\mathbf{x}, \zeta)$ and thus the magnigfication is not unique. However, $\sigma(\mathbf{x}, \zeta)$ can be interpreted as the stress that one obtains if the true microscopic normal stress is averaged over an area $(\mathcal{L}/\zeta)^2$, which has its center of mass located at the lateral position $\mathbf{x}$. By definition, the probability distribution $P(\sigma, \zeta + \Delta\zeta)$ of the normal stress at magnification $\zeta + \Delta\zeta$ is:

$$P(\sigma, \zeta + \Delta\zeta) = \langle \delta\{\sigma - \sigma(\mathbf{x}, \zeta + \Delta\zeta)\} \rangle \,, \qquad (3)$$

where the average $\langle \cdots \rangle$ is an average over different surfaces. When changing the magnification, the coarse-grained stress will change as well, which can be expressed as:

$$\sigma(\mathbf{x}, \zeta + \Delta\zeta) = \sigma(\mathbf{x}, \zeta) + \Delta\sigma(\mathbf{x}, \zeta, \Delta\zeta), \qquad (4)$$

where $\Delta\sigma(\mathbf{x}, \zeta, \Delta\zeta)$ is the (local) change in stress upon a change in magnification from $\zeta$ to $\zeta + \Delta\zeta$. Expressing the expectation value $\langle \cdots \rangle$ with an ensemble average $\frac{1}{N}\sum_i$ over a set of random surfaces, where $i$ enumerates the different realizations of the random surface and an integral over the full surface $A_0$, and inserting Eq. (4), we can rewrite Eq. (3) as

$$P(\sigma, \zeta + \Delta\zeta) = \frac{1}{N} \sum_{i=1}^{N} \frac{1}{A_0} \int d^2x \, \delta\{\sigma - \sigma_i(\mathbf{x}, \zeta) - \Delta\sigma_i(\mathbf{x}, \zeta, \Delta\zeta)\}, \qquad (5)$$

where $\sigma_i(\mathbf{x}, \zeta)$ is the microscopic stress in realization $i$, at position $\mathbf{x}$ and magnification $\zeta$. It is now possible to replace the ensemble average over $i$ with an average over the various values that $\Delta\sigma$ can take. The probability distribution $\Pr(\Delta\sigma)$ can, and in most cases will, be a function of the macroscopic stress $\sigma_0$, the local stress $\sigma$, and of course, the rules for generating the random height function $h(\mathbf{x})$, as well as the rules for the calculation of $\sigma(\mathbf{x}, \zeta)$. However, due to translational invariance induced by the ensemble averaging, $\Pr(\Delta\sigma)$ will not depend on the lateral coordinate $\mathbf{x}$. We can therefore rewrite Eq. (5) as

$$\begin{aligned} P(\sigma, \zeta + \Delta\zeta) \;&=\; \int d(\Delta\sigma) \Pr(\Delta\sigma) \\ &\quad \times \frac{1}{A_0} \int d^2x \, \delta\{\sigma - \Delta\sigma - \sigma_i(\mathbf{x}, \zeta)\}, \end{aligned} \qquad (6)$$

which can be identified as

$$P(\sigma, \zeta + \Delta\zeta) = \int d(\Delta\sigma) \Pr(\Delta\sigma) P(\sigma - \Delta\sigma, \zeta), \qquad (7)$$

provided that $A_0$ is sufficiently large to be self averaging. We will now discuss some properties of $\Pr(\Delta\sigma)$. For all values of $\Delta\zeta$, one may require that $\int_{-\infty}^{+\infty} d(\Delta\sigma) \Pr(\Delta\sigma)$ be unity. Moreover, $\Pr(\Delta\sigma)$ must produce a vanishing first moment of $\Delta\sigma$ on average, because the average normal stress is independent of the level of magnification. However, since $\Pr(\Delta\sigma)$ is a conditional probability, e.g., it can depend on $\sigma$ in principle, $\langle \Delta\sigma \rangle$ does not necessarily vanish for each individual value of $\sigma$. However, to simplify the analysis we will assume that $\langle \Delta\sigma \rangle = 0$ for every value of $\sigma$. The validity of this approximation will be discussed in a separate paper.

The knowledge of the leading moments of $\langle \Delta\sigma^n \rangle$ are useful when expanding $P(\sigma - \Delta\sigma, \zeta)$ into a second-order Taylor series with respect to $\Delta\sigma$, i.e., for small values of $\Delta\zeta$, the right-hand side of Eq. (7) simplifies to $P(\sigma, \zeta) + [\partial^2 P(\sigma, \zeta)/\partial\sigma^2] \times \langle \Delta\sigma^2 \rangle$, where $\langle \Delta\sigma^2 \rangle$ denotes the expected mean square change of $\sigma$ when changing the

magnification from $\zeta - \Delta\zeta$ to $\zeta$. Expanding the left-hand side of Eq. (7) into a first-order Taylor series with respect to $\Delta\zeta$ finally yields

$$\frac{\partial P}{\partial \zeta} = \frac{1}{2}\frac{\langle \Delta\sigma^2 \rangle}{\Delta\zeta}\frac{\partial^2 P(\sigma,\zeta)}{\partial^2 \sigma}. \tag{8}$$

For the equation to be usable, it is necessary to find an expression for the function

$$D(\zeta, \sigma, \sigma_0, ...) = \frac{1}{2}\frac{\langle \Delta\sigma^2 \rangle}{\Delta\zeta}, \tag{9}$$

which can be associated with a diffusion constant. $D$ will depend, as alluded to above, on $\sigma$, $\sigma_0$, the rules for coarse-graining normal stress as well as those for the generation of the random profile $h(\mathbf{x})$ and the mechanical properties of the solids. The difficulty is to find good approximations for $D$.

In the original treatment, Persson coarse-grained the description of the normal stress in reciprocal space by defining an upper cutoff in wavelength. We follow this procedure here. The idea is that smearing out the stress in real space over a linear length $\mathcal{L}/\zeta$ is equivalent to defining an upper cutoff in reciprocal space at $\zeta q_0$, with $q_0 = 2\pi/\mathcal{L}$. The expected squared variance in $\Delta\sigma$ can then be calculated from

$$\begin{aligned} \langle \Delta\sigma^2 \rangle &= \int_{q_0\zeta}^{q_0(\zeta+\Delta\zeta)} d^2q \left\langle \tilde{\sigma}(\mathbf{q})^2 \right\rangle \\ &= 2\pi\Delta\zeta \cdot q_0 \cdot (\zeta q_0) \cdot \left\langle \tilde{\sigma}(\zeta q_0)^2 \right\rangle . \end{aligned} \tag{10}$$

In linear response, $\sigma$ and the displacement field $u$ are connected linearly via an equation of the form $\tilde{\sigma}(\mathbf{q}) \propto q\tilde{E}(\mathbf{q})\tilde{u}(\mathbf{q})$ where $\tilde{E}$ is some generalized elastic constant.

The rather blunt assumption now is that for the parameterization of the constitutive term $\langle \Delta\sigma^2 \rangle / 2\Delta\zeta$, it is possible to replace $\tilde{u}(\mathbf{q})$ with the height profile $\tilde{h}(\mathbf{q})$ in the $\sigma(\mathbf{q}) \propto \tilde{u}(\mathbf{q})$ relation. This approximation yields

$$\left\langle \tilde{\sigma}(\mathbf{q})^2 \right\rangle = q^2 |E'|^2 \left\langle |\tilde{h}(\mathbf{q})|^2 \right\rangle / 4 \tag{11}$$

with $E' = E/(1-\nu^2)$, $E$ being the elastic modulus and $\nu$ being the Poisson ratio. Thus, $D$ defined in Eq. (9) can be written as

$$D = \frac{\pi}{4}\zeta^3 q_0^4 |E'|^2 \left\langle |\tilde{h}(\zeta q_0)|^2 \right\rangle \tag{12}$$

where we have assumed that the stochastic properties of the height profile are rotationally isotropic, i.e., the variance in $\tilde{h}(\mathbf{q})$ only depends on the magnitude of $\mathbf{q}$. It is interesting to note that the diffusion coefficient does not depend on $\sigma$ in the given approximation, which facilitates the solution of the partial differential equation for $P(\sigma, \zeta)$. If no constraints on the stress diffusion are applied, the solution for $P(\sigma, \zeta)$ would be analogous to the solution of the diffusion equation. Hence, the solution would be

$$P(\sigma, \zeta) = \frac{1}{\mathcal{N}} \exp\left\{ -\frac{(\sigma - \sigma_0)^2}{4\int_1^\zeta d\zeta' D(\zeta')} \right\} \tag{13}$$

with the normalization constant

$$\mathcal{N} = \sqrt{4\pi \int_1^\zeta d\zeta' D(\zeta')}. \tag{14}$$

If the walls are purely repulsive, stresses can only be greater than or equal to zero. This constraint can be taken into consideration with the boundary condition $P(\sigma < 0, \zeta) = 0$, i.e., $\sigma = 0$ plays the role of an absorbing boundary. The constraint $P(\sigma < 0, \zeta) = 0$ can be incorporated with a method of image charges, [15] i.e., one Gaussian (or $\delta$ function peak) with positive amplitude is placed at $\sigma = L/A$ and an equivalent peak with negative amplitude is placed at $\sigma = -L/A$. The width of both Gaussians is then treated according to the scheme described in Eqs. (13) and (14).

### B. Extension to load-bearing particles

The special topography of the aluminum silicon alloys makes it obvious that load will only be carried on the silicon particles. Thus the only roughness (or mean-gradients) that should enter the calculations should be the roughness associated with the silicon particles. The "depth" of the aluminum valleys and the roughness in those valleys will most certainly not influence the pressure distribution. This insight asks for a generalization for the measure of height-fluctuations that enter Persson theory.

We pursued two approaches that project on the roughness of the silicon particles. One approach is local, i.e., stress fluctuations are related to height-gradients on the silicon particles, the other one is non-local and potentially more promising. Within the local approach, one would compute the stress according to the equation $\sigma = E'\nabla h/2$ on the silicon-rich particles and set it to zero otherwise. This procedure would yield the following stress correlation function

$$\langle \sigma(\mathbf{x})\sigma(\mathbf{x}') \rangle = \left(\frac{E'}{2}\right)^2 \langle \{\nabla h(\mathbf{x}) \Theta_{\mathrm{Si}}(\mathbf{x})\} \{\nabla h(\mathbf{x}') \Theta_{\mathrm{Si}}(\mathbf{x}')\} \rangle, \tag{15}$$

where $\Theta_{\mathrm{Si}}(\mathbf{x}) = 1$ on top of the silicon particles, while it is zero in the aluminum valleys. Note that Eq. (15) is the real space analogue or generalization of Eq. (11), which is formulated in reciprocal space.

The disadvantage of the local generalization is that it does not contain any information about height-differences between different load-bearing entities. We therefore considered an alternative approach, which is based on a generalized height-difference correlation function defined as:

$$C_2(R) = \frac{\int d^2x d^2x' \delta(R - \Delta r) \Theta_{\mathrm{Si}}(\mathbf{x}) \Theta_{\mathrm{Si}}(\mathbf{x}') \{h(\mathbf{x}) - h(\mathbf{x}')\}^2}{\int d^2x d^2x' \delta(R - \Delta r) \Theta_{\mathrm{Si}}(\mathbf{x}) \Theta_{\mathrm{Si}}(\mathbf{x}')} \tag{16}$$

with $\Delta r = |\mathbf{x} - \mathbf{x}'|$. $C_2(R)$ states the expected standard deviation in height as a function of distances $R$ under the condition that silicon particles are at the origin $\mathbf{x}$ as well as at the destination $\mathbf{x}'$. Note that this expression is equivalent to a regular height-difference auto correlation function if the surface consists only of silicon.

Once $C_2(R)$ is constructed, we suggest exploiting the regular relations for height-difference correlation functions. These relations enable one to calculate mean-square gradients associated with the correlation function $C_2(R)$, i.e., it is possible to compute the generalized expressions for $\left\langle |\tilde{h}(\mathbf{q})|^2 \right\rangle$ from which the stress histograms for the magnification of interest can be computed. If we want to know the pressure distribution at a mesoscopic length scale $\lambda_\mathrm{m}$, say a length scale close to the mean separation between silicon particles, then we integrate Eq. (13) only up to magnifications associated with wavenumbers $2\pi/\lambda_\mathrm{m}$. The relevant relations for the Fourier transforms will be provided in appendix A.

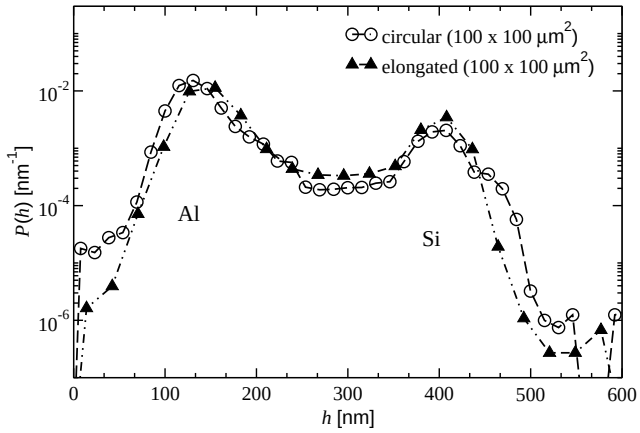


FIG. 3: Height distribution $P(h)$ for the two investigated Al-Si samples.

## IV. RESULTS

### A. Surface characterization

Contact mechanics strongly depends on the topography of the surfaces. Theories use surface characterization as an input to predict stress distributions and contact areas. For example, Greenwood-Williamson (GW) type models [9] are based on asperity height and curvature statistics, while Persson theory is based on two-point correlation functions. Neither information is sufficient to fully reconstruct the stochastic information on the surfaces' topography, which implies that information contained in neither asperity statistics nor two-point correlation function is sufficient to rigorously predict stress distributions. Thus neither theory can claim legitimately to be generally exact. Yet, the information contained in asperity statistics or in two-point correlation function is important because it seriously constrains what the real topography and hence the contact mechanics can be.

We will start our surface characterization with the surfaces' height distribution, which is shown in Fig. 3. Two peaks occur. The one at small heights can be identified with the aluminum matrix, while the peak at larger heights is related to the silicon particles. The two peaks are separated by about 300 nm for both alloys. Subtle differences can be seen in the tails of the height distribution at large values of the height $h$, i.e., the surfaces of the alloy producing the more circular-shaped asperities appears to have the broader tail.

In order to investigate the subtle differences in the tails of $P(h)$ further, we also calculated the height distributions of individual silicon particles. The circular particles had a much greater propensity to have highly polished tops, i.e., the $P(h)$ of individual particles drops abruptly at large values of $h$. Conversely, the material with elongated particles has both highly polished and barely polished particles, i.e., the $P(h)$ of individual particles sometimes decreases rather slowly at large values of $h$. This observation can be understood as follows: in terms of bulk property, material A1934 with its higher silicon content and other hard intermetallic phases is harder than A1955. Thus, A1934 is less susceptible to polishing than 1955, because the polishing was done under the same loading condition, resulting in the larger degree of polishing observed in A1955. In terms of surface property, the exposed particles in material A1934 contain both Si and other intermetallic phases, which have different resistance to polishing. Thus a larger variation of the surface roughness on these particles were found.

Besides the differences in morphology and height distribution between the two samples, there are also differences related to the in-plane order. This becomes apparent when analyzing the silicon-silicon distribution function $g_\mathrm{SiSi}(r)$, which states the probability to be on top of a silicon particle at a distance $r$ if the origin is placed on a silicon particle itself. Note that in the limit $r \to \infty$, $g_\mathrm{SiSi}(r)$ becomes identical to the relative area that the particles occupy on top of the aluminum matrix. A comparison for the two samples is shown in Fig. 4.

Both samples show interesting features in $g_\mathrm{SiSi}(r)$, which reflect the difference in microstructure bewteen hypoeuctectic and near-eutectic melts after solidification. For material A1955, the $g_\mathrm{SiSi}(r)$ decays in a two-step process. This is due to the circular particles having a somewhat bi-modal distribution with one eutectic Al-Si area surrounded by a few pro-eutectic aluminum domains (i.e., a dendritic aluminum microstrucre). The first step in $g_\mathrm{SiSi}(r)$ corresponds to finding silicon within the eutectic area, and the second step to finding silicon beyond the pro-eutectic aluminum grains. The load-bearing particle distribution is more homogeneous for near eutectic material, since most of all silicon and aluminum phases crystallized at the same time at the eutectic composition.

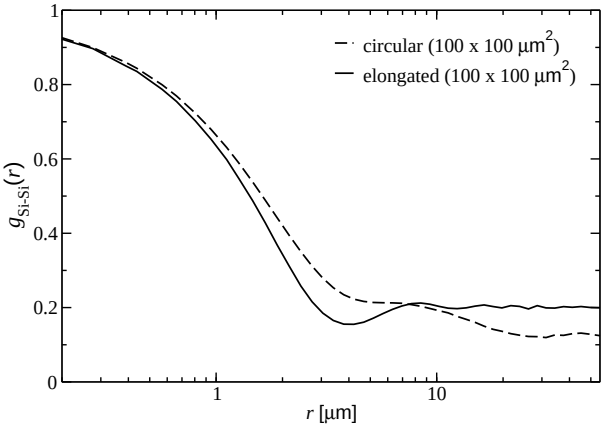


FIG. 4: Silicon-silicon correlation function $g_{\mathrm{SiSi}}(r)$ for surfaces bearing circular and elongated particles.

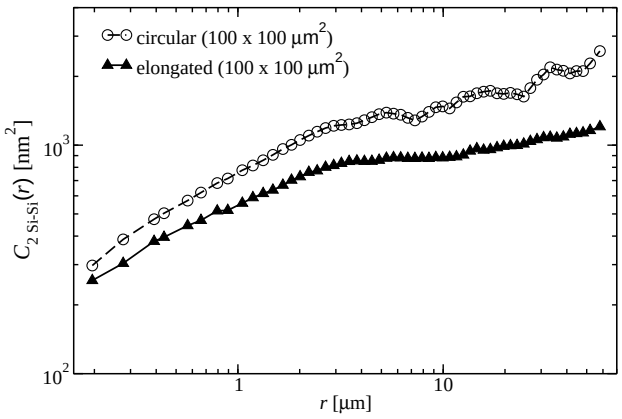


FIG. 5: Height-difference correlation function $C_2(r)$ for the two investigated samples. Note that only those height differences are taken into consideration where origin and destination are located on silicon particles.

The $g_{\mathrm{SiSi}}(r)$ goes through a minimum before reaching its $r \to \infty$ plateau value, indicating that it is unlikely to find another silicon particle at a 4 $\mu$m distance. This is consistent with the spacing between eutectic Si particles, which is typically on the same order of their particle size.

To complete our surface characterization, we show the silicon-projected height-difference autocorrelation function $C_2(R)$ in Fig. 5, see also Eq. (16) where $C_2(R)$ is defined. The correlation functions can be described roughly as follows: At distances $r < 3$ $\mu$m, i.e., on the silicon-rich particles, $C_2$ grows with a powerlaw. The Hurst roughness exponent $H$ would be rather small, i.e., $H \approx 0.2$. ($H$ is frequently used to approximate $C_2(R)$ with a powerlaw $\propto R^{2H}$. For a regular random walk, $H = 1/2$ holds. Smaller values of $H$ indicate an increased short-wavelength roughness.) At distances $r > 10$ $\mu$m, i.e., if height differences are evaluated between two different particles, $C_2$ grows even more slowly, and though no clear power law is evident, one could argue that the growth of the height-difference correlation function would be roughly consistent with a Hurst roughness exponent $H \approx 0.1$. Note that the values for $C_2(r)$ at large values of $r$ are approximately the squared widths of the height distributions of those peaks in $P(h)$ (see Fig. 3) that are associated with silicon particles.

### B. Contact characterization

Knowing the topography of the surfaces does not allow one to determine where contact is going to take place. When a rough surface is pressed against a flat counter surface the highest point of the rough surface will make contact first, whereby the vicinity of this point will be pushed down and hence perturb the local topography. Local overlap models ignore this coupling and thus predict areas where contact takes places that are too clustered. For self-affine contacts, this elastic coupling makes the contact morphology different than what one would obtain from an asperity-overlap model. [16] Here we would like to investigate whether a similar statement holds when the surfaces have roughness on disparate length scales.

Figure 6 contrasts the contact morphology that we obtain for a normal macroscopic pressure of 5 MPa to that which we would have obtained in an overlap model. For this comparison, we assumed that an overlap model would produce the same relative area of contact as that found in the numerically-exact GFMD calculations. As expected, contact is spread over more particles in the numerically exact calculations that include long-range elasticity than if contact had occurred merely based on local height differences.

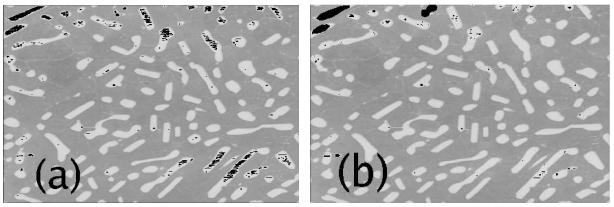


FIG. 6: View of the Al-Si surface. White areas indicate silicon particles, while grey areas correspond to the aluminum matrix. Black points mark the microscopic points of contact. The total area of contact accounts to 0.66%. The normal macroscopic pressure would correspond to 5 MPa, i.e., $p_{\mathrm{macro}} = 0.11 \times 10^{-3}$ in our dimensionless units. Figure (a) is the full GFMD calculation, while (b) is the prediction by an overlap model.

To quantify the results presented in Fig. 6 further, we calculated the contact autocorrelation function $g_{\mathrm{cc}}(r)$, which is shown in figure 7 for two different relative contact areas. $g_{\mathrm{cc}}(r)$ states the probability of having con-

tact at a distance $r$ from the origin if there is contact at the origin. While our statistics are rather limited, we still feel confident to draw the following conclusions: The overlap model significantly overestimates the correlation to have contact at a distance $r$ if there is contact in the origin. It even appears that the overlap model does not reproduce the correct behavior for large $r$, as long as $r$ is less than the longest wavelength on which roughness is found. In both cases, i.e., 0.66% and 10% contact ratio, does the overlap model fail to show the correct "pseudo-asympotic" behavior, which, as revealed by the GFMD calculations, would consist of $g_{\rm cc}(r)$ approaching the value of $A/A_0$ at relatively small values of $r$. (Here, "pseudo-asymptotic" behavior referes to the behavior of a function for arguments that are large compared to the mesoscopic lengthscales, but smaller than the longest wavelength on which roughness is found.) The dip in the overlap model for values of $r$ close to half the simulation cell can be rationalized as follows: The integral of $g_{\rm cc}$ over the (periodically repeated) domain must be exactly equal to the real area of contact $A$. Since overlap models grossly overestimate contact near the highest peak, this strict requirement can only be satisfied with the dip at large values of $r$. We suspect that overlap models are generally unable to produce the correct pseudo-asymptotic behavior for contact correlation functions. This claim is also supported by the observation that the Fourier transform of the contact correlation function as predicted by the overlap models does not show the correct scaling at small wavenumbers, see figure 6 in Ref. 16.

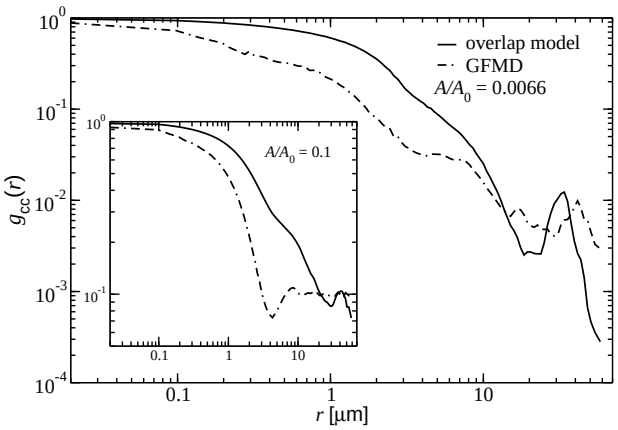


FIG. 7: Contact autocorrelation function $g_{\rm cc}(r)$ from GFMD and from an overlap model. The relative contact area $A/A_0$ is 0.66% in the main figure and 10% in the inset.

Given our interpretation of our Fig. 7, we conclude that it is not possible to reliably predict the distribution of forces on individual particles with overlap models even if we had an exact relation for load and displacement at the single-particle level. First, one would not pick all the correct particles that experience a non-zero external load and thus sample the wrong set of particles. Second, those asperities that would be identified correctly would be subjected to a force that is too large.

### C. Stress distributions

In this section, we will present the results of our contact mechanics GFMD calculations and try to rationalize the results within the context of our analysis of the surface topographies. In our calculations, the net load exerted was varied such that the corresponding macroscopic pressures fell in the range of 1.3 KPa to 0.9 GPa. As the surface coverage of silicon particles is approximately 13% and 20% for A1955 and A1934, respectively, the average mesoscopic stress will be approximately five to eight times larger than the macroscopic stress assuming all particles are in contact. The distribution of microscopic stresses is more difficult to ascertain than that of mesoscopic pressures, because computing microscopic stresses requires a fine resolution of mesh points for the whole system.

#### 1. *Pressure and its distribution in individual particles*

Before presenting the results for the probability distribution, it is worth visualizing the pressure in single asperity contacts. Characteristic differences can be recognized in Fig. 8 between circular and elongated asperities. The circular particles carries significant load on its rims and the effect of polishing is clearly evidenced by "ridges." Conversely, the elongated particle does not have increased pressures at its rim and height fluctuations can be related to "asperities" that reside on top of the particle rather than to trenches produced through polishing. This behavior can be understood from the observation that the material A1934 has the more abruptly ending tops, see the discussion following Fig. 3, i.e, the pressure distribution on circular particles resemble the "flat-punch" continuum solution more closely than that of the elongated particles. We remind the reader that the continuum solution for $P(p)$ of a flat punch shows a square root singularity at the punch edge. [17]

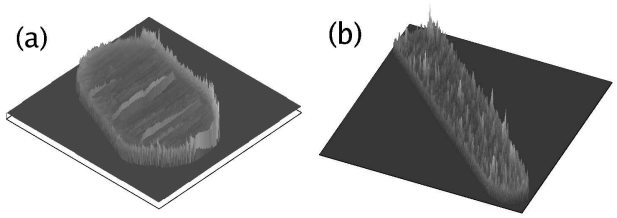


FIG. 8: Local pressure in (a) a (quasi) circular and (b) an elongated particle. Bright and dark colors indicate areas of high and low local pressure, respectively.

A statistical analysis of the pressures visualized in Fig. 8 is made in Fig. 9. For both particles, there is an exponential tail in the pressure distribution. Such tails have

been identified previously for experimentally-determined rough height profiles, as opposed to those computed for artificially created height profiles. [18] Only the artificial height profiles produced Gaussian tails in agreement with Persson's theory. It is surprising that the same characteristics, that is, exponential tails, are borne out for relatively small single-asperity particles as for distinctly larger, self-affine contacts.

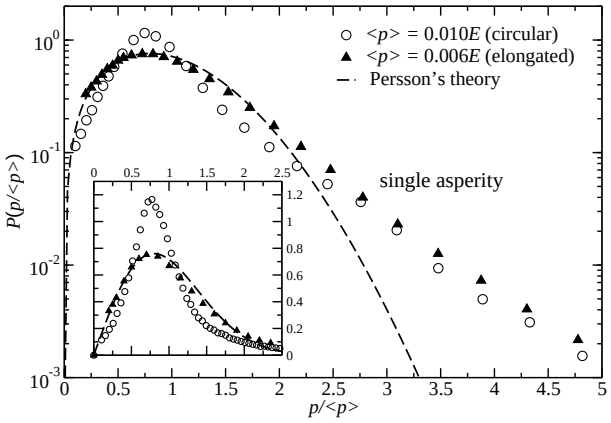


FIG. 9: Distribution function for microscopic pressures, $P(p_{\rm micro})$ for circular and elongated particles. The applied macroscopic pressure would correspond to 65 MPa in real units and 0.0015 in reduced units. Inset: same distributions on a linear scale.

The deviation in $P(p)$ from a Gaussian distribution can be rationalized as follows: The stress-independence of the ratio $\langle\Delta\sigma^2\rangle/\Delta\zeta$, see Eqs. (8), is motivated by the assumption that $\tilde{h}(\mathbf{q})$ and $\tilde{h}(\mathbf{q}')$ are stochastically independent for $\mathbf{q} \neq \mathbf{q}'$. Real surfaces, however, show correlation in their height spectra. This correlation will lead to a $\sigma$-dependent ratio $\langle\Delta\sigma^2\rangle/\Delta\zeta$, so that the solutions for $P(\sigma)$ do not need to be Gaussian any longer.

Although Persson's pressure distribution is Gaussian (or the superposition of two Gaussians), it is worth comparing the computed and predicted distribution on a linear scale. The comparison is shown in the inset of Fig. 9. In the case of elongated particles the agreement is rather impressive, despite the fact that the theory does not address the tails properly. The agreement is not as good for the circular asperities, which can be understood from the observation that the rim carries significant load. Moreover, the theory assumes isotropy, while the circular asperity shows ridges, probably due to more extensice polishing.

### 2. *Distribution of pressure in multi-particle contact*

As mentioned various times in this paper, stress distributions depend on the level of magnification in which they are accumulated, the finer the scale the larger the mean pressure. Of particular interest for Al-Si alloys is the load distribution on individual particles, as well as the microscopic stress distributions. Exemplary results are shown in Fig. 10. It is clear that the local stress can be an order of magnitude larger than the applied macroscopic stress. The average mesoscopic stress will be approximately five to eight times larger than the macroscopic stress assuming all load-bearing particles are in contact. And the microscopic pressure due to the finest roughness on the Si surfaces, can be 100 1000 times larger.

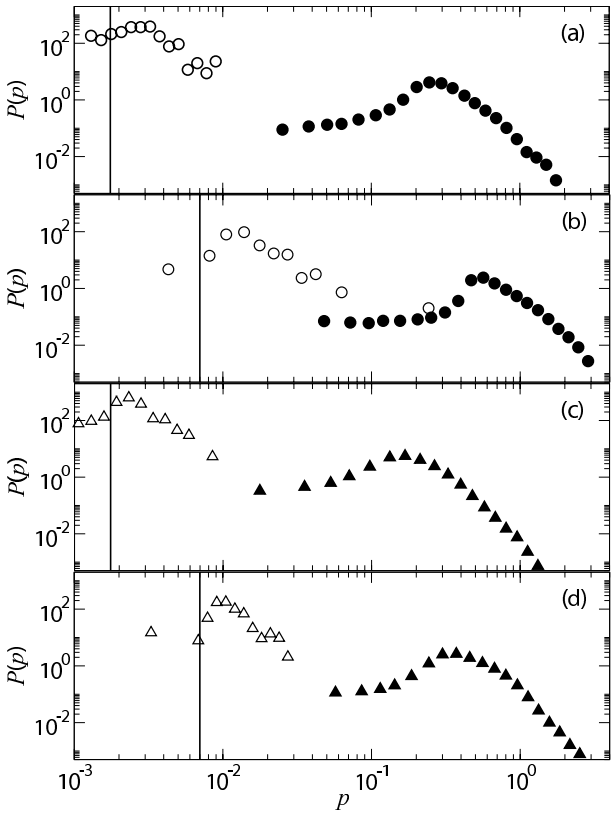


FIG. 10: Macroscopic, mesoscopic, and microscopic pressure distribution for different external, nominal pressures. Figures (a), (b) and (c), (d) refer to A1955 and A1934 materials, respectively. Lines denote the macroscopic pressure, open symbols the stress distribution at the mesoscopic scale, see equation 2, and closed symbols are used for the microscopic stress distribution.

It is worth commenting on the broad tails of the microscopic pressures at small values of $p$ in figure 10. These tails are artifacts of the finite discretization of our elastic manifold. In fully converged calculations, $P(p)$ would tend to zero rather than to a constant at small values of $p$. While it would be desirable to further decrease the discretization, we wish to note that it is currently outside of our feasibility to do so. Specifically, we begin the calculations with $N = 1024 \times 1024$ grid points for the full surface. In this simulation, we ascertain the load on individual particles, from which the mesoscopic stress distribution is derived. In a second series of simulations,

individual particles are randomly-chosen and the previously ascertained loads are applied to them. The number of grid points is again $N = 1024 \times 1024$, however a much smaller area needs to be simulated. In a previous paper, [18] we showed that mean microscopic pressure and contact area could be calculated accurately if use was made of finite-size extrapolation, which is why a third simulation with $N = 512 \times 512$ discretization was run.

From calculations like those presented in Fig. 10, it is possible to ascertain the mean pressures at a mesoscopic and microscopic scale, which are shown in Fig. 11. Only A1934 was shown as an example. The load $L$ is normalized by the contact area and the materials' modulus. Fig. 10 shows that the mean microscopic pressure barely changes with the external load. Also the mean mesoscale pressure is relatively constant within a certain window, however, at both very large and very small external loads, $\langle p_{\mathrm{meso}} \rangle$ is linear in $L$. This observation can be rationalized as follows: For small $L$, there is only one silicon particle in contact, which carries all the load. For large $L$, all particles carry load, and the mean mesoscopic pressure becomes the load divided by the net surface covered by the particles. The mean pressure is relatively flat in between these two limits.

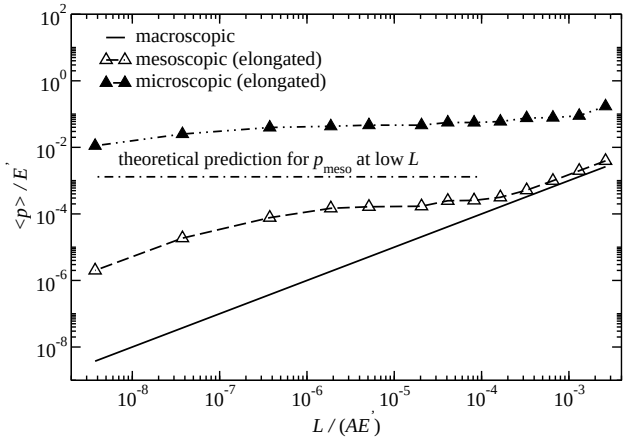


FIG. 11: Mean microscopic, mesoscopic, and macroscopic pressure as a function of the external load for a surface covered with predominantly elongated particles.

The weak dependence of the mean mesoscopic pressure is consistent with the observation that there is some residual roughness at mesoscopic length scales. This roughness at the mesoscale becomes evident in the silicon-projected height-difference correlation function $C_2(r)$. Of course, it would be desirable to have the ability to predict the plateau value for the mesoscopic pressure. In section III B, we argued how to modify Persson theory to the case where the load is carried only by silicon particles. Applying these modifications to the current calculations and cutting off roughness at wavelengths of roughly 10 $\mu$m, leads to a mesoscopic pressure that is about 20 times larger than the pressures that were actually computed from GFMD. Inspection of figure 6 reveals that most particles that we count as being in contact only have a marginal part of their surface in contact. These asperities reduce the mean pressure quite substantially and may thus contribute to the discrepancy between theoretical description and numerical results.

## V. SUMMARY AND CONCLUSIONS

In this study, we investigated the contact mechanics of two Al-Si alloys with Green's function molecular dynamics. The microstructural differences between the two alloys lead to characteristic geometries of the silicon-rich domains. These domains become particles that stick out of the surface after appropriate surface treatments. In one case, material A1955, the particles are typically closer to a circular shape than for material A1934, which shows rather elongated particles. The particles are supposedly the load-bearing entities during mechanical contact.

Our study included an analysis of various correlation functions that describe the topography of free surfaces, the geometry of those places where microscopic contact occurs, as well as the pressure distributions both on a microscopic scale but also on a mesoscopic scale, i.e., on a length scale associated with the typical spacing between asperities. Whenever appropriate, comparison was made to either overlap models, which enter, for instance, Greenwood-Williamson theory, or to Persson's contact mechanics theory.

In our calculations, some quantitative and qualitative differences between the two alloys became apparent. First, the two alloys appear to have a different response to polishing. Specifically, the pressure profiles on particles of material A1955 show more similarity to the "flat-punch continuum solution" than the material A1934. Second, the differences in height on top of the particles increases more quickly with distance for material A1955 than for A1934. Third, the microscopic pressure distribution for material A1934 follows Persson's contact mechanics theory much better than that of material A1955. Fourth, the mean microscopic pressure is larger for A1955 than for A1934. This last observation can be explained by the fact that, as compared to A1955, material A1934 has the smaller roughness at the smallest length scales.

In this paper, we also attempted to generalize Persson's theory to the case where load can only be carried on places known a priori, specifically, where load can only be carried on silicon particles. The goal of these calculations was to ascertain what average load one should expect on a load-bearing particle of a given area. For the system analyzed, our generalization of Persson's theory predicts pressures that are off by about a factor of twenty from our numerical results. Unfortunately, overlap models will not be in a position to yield better results. Analysis of the geometry of those areas where contact takes place revealed that overlap models produce contact mainly in the

vicinity of the highest particle, while load was distributed much more evenly across the surface once elastic deformation was incorporated by the GFMD calculations.

Despite the failure of overlap models to produce correct contact geometries, they are still useful to rationalize why the mesoscopic stress, which we defined to be the pressure averaged over all particles in contact, remains constant over a relatively broad pressure range. When increasing the external load, those particles that are already in contact will carry larger loads, however new particles come into contact, which initially carry little load but immediately "contribute" their full area of contact to the calculation. Unfortunately, neither overlap models nor Persson theory are able to reliably predict what the load is that an individual particle has to carry. This leaves us to conclude that at the present stage of theory, predicting the contact mechanics of Al-Si surfaces requires numerical solutions of the models, even when the models are at the rather simplified level considered here, i.e., static contacts, use of the harmonic approximation and absence of any lubricant, homogeneous elastic approximation, and neglecting plasticity and particle fracture.

Despite the limitations of our model, there are implications of how the information on both mesoscopic pressures and microscopic pressures contained in the GFMD results can be interpreted to analyze real contacts with aluminum silicon alloys. The wisdom associated with including hard phases in aluminum alloys destined for tribological applications is that the exposed hard phases will support the applied load, and prevent the counterface from coming into direct contact with the aluminum matrix. Knowing the forces on individual particles and the associated distribution of mesoscopic pressures helps one design an alloy and a contact with a reasonable safety factor to avoid aluminum adhesion. The GFMD simulation of the microstructures presented here shows that the predicted pressure distribution has a dependence on $L/(AE)$, which is not captured by overlap models or our extension of Perssons theory. Both Persson and overlap model overestimate the load carried by individual particles.

The knowledge of microscopic pressure distribution is relevant to the fracture of silicon particles. The GFMD calculations show that there is a significant contribution to the pressure distribution at high pressures, which is not captured by Persson's analytic theory. GW models cannot be applied to the particular shape of the silicon particles, but they usually also show Gaussian tails in the pressure distribution and would thus suffer from the same shortcoming as Persson's theory. From a practical point of view, this teaches us that smoother particles (by polishing) with rounded edges will minimize the pressure distribution components that can lead to hard phase fracture, which is known to be a failure mechanism in sliding contact of similar surfaces.

## APPENDIX A: MATHEMATICAL APPENDIX

In this appendix, we provide the formulae necessary to transform a correlation function with radial symmetry into reciprocal space and to transform them back with a cutoff in wavenumber. Let us chose a symmetric Fourier transform, i.e.,

$$\tilde{h}(\mathbf{q}) = \frac{1}{2\pi}\int_{-\infty}^{+\infty} d^2x\, e^{i\mathbf{qx}} h(\mathbf{x}) \tag{A1}$$

and the inverse transform

$$h(\mathbf{x}) = \frac{1}{2\pi}\int_{-\infty}^{\infty} d^2q\, e^{-i\mathbf{qx}} \tilde{h}(\mathbf{q}). \tag{A2}$$

Let us furthermore assume stochastically independent fluctuations in $\tilde{h}$ for different values of $\mathbf{q}$, i.e.,

$$\left\langle \tilde{h}(\mathbf{q})\tilde{h}(\mathbf{q}')^* \right\rangle = 2\pi\tilde{C}(\mathbf{q})\delta(\mathbf{q}-\mathbf{q}') \tag{A3}$$

Then with these definitions, the correlation function

$$C(\Delta\mathbf{x}) = \langle h(\mathbf{x})h(\mathbf{x}+\Delta\mathbf{x})\rangle \tag{A4}$$

can be shown to be the (inverse) Fourier transform of $\tilde{C}(\mathbf{q})$, which implies that

$$\tilde{C}(\mathbf{q}) = \frac{1}{2\pi}\int_{-\infty}^{\infty} d^2x\, e^{-\mathbf{qx}} C(\mathbf{x}). \tag{A5}$$

When $C(\mathbf{x})$ is a function of $x = |\mathbf{x}|$, the last equation can be rewritten as

$$\tilde{C}(\mathbf{q}) = \int_0^{\infty} dx\, x\, C(x) \left\{ \frac{1}{2\pi}\int_0^{2\pi} d\varphi\, e^{-iqx\cos\varphi} \right\} \tag{A6}$$

The expression in the curly brackets is the Bessel function of the first kind $J_0(qx)$. From that equation it becomes clear that $\tilde{C}(\mathbf{q})$ only depends on $q = |\mathbf{q}|$, so that one can calculate the expectation value of the r.m.s. gradient $G$

$$\begin{aligned} G &= \langle \nabla h(\mathbf{x}) \nabla h(\mathbf{x})\rangle \\ &= \frac{1}{(2\pi)^2}\int_{-\infty}^{+\infty} d^2q\, d^2q' (-i\mathbf{q})(+i\mathbf{q}') e^{-i\mathbf{qx}} e^{i\mathbf{qx}'} \left\langle \tilde{h}(\mathbf{q})\tilde{h}^*(\mathbf{q}') \right\rangle \\ &= \frac{1}{2\pi}\int_{-\infty}^{+\infty} d^2q\, d^2q' (-i\mathbf{q})(+i\mathbf{q}')\tilde{C}(\mathbf{q})\delta(\mathbf{q}-\mathbf{q}') \qquad \text{(A7)} \\ &= \frac{1}{2\pi}\int_{-\infty}^{\infty} d^2q\; q^2\; C(\mathbf{q}) \qquad \text{(A8)} \end{aligned}$$

Since $C(\mathbf{q})$ only depends on $q$, this can be simplified to

$$G = \int_0^{q_c} dq\, q^3 C(q), \tag{A9}$$

where a finite cutoff $q_c$ was introduced in frequency space.

[1] J. R. Davis. Friction and wear of internal combustion engine parts, in friction, lubrication, and wear technology. In *ASM Handbook 10th ed., vol. 18*, pages 553–562. ASM International, Materials Park, OH (1992).

[2] R. E. Green. Die casting the vega engine block. *Die Cast Engineer*, 14:12–26, 1970.

[3] J. L. Jorstad. The hypereutectic aluminum silicon alloy used to cast the vega engine block. *Modern Castings*, 60:59–61, 1971.

[4] A. T. Alpas A. R. Riahi, T. Perry. *Mater. Sci. Eng. A*, 343:76, 2003.

[5] R. L. Deuis, C. Subramanian, and J. M. Yellup. Dry sliding wear of aluminium composites - a review. *Sci. and Tech.*, 57:415, 1994.

[6] S. A. Reddy, B. N. Pramila Ba, K. S. S. Murthy, and S. K. Biswas. Wear and seizure of binary al-si alloys. *Wear*, 171:115, 1994.

[7] M. Chen, T. Perry, and T. A. Alpas. Ultra-mild wear in eutectic AlSi alloys. *Wear*, 263:552, 2007.

[8] C. Campañá and M. H. Müser. *Phys. Rev. B*, 74:075420, 2006.

[9] J. A. Greenwood and J. B. P. Williamson. *Proc. Roy. Soc. Lond.*, A295:300, 1966.

[10] Das, T. Perry, and S.K. Biswas. Effect of surface etching on lubricated sliding wear of an eutectic "al-si" alloy. *Tribol. Lett.*, 21:193, 2006.

[11] J. Hoshen and R. Kopelman. *Phys. Rev. B*, 14:3438, 1976.

[12] B. N. J. Persson. *J. Chem. Phys.*, 115:3840, 2001.

[13] B. N. J. Persson, O. Albohr, U. Tartaglino, A. I. Volokitin, and E. Tosatti. *J. Phys.: Condens. Matter*, 17:R1, 2005.

[14] B. N. J. Persson. *Surf. Sci. Rep.*, 61:201, 2006.

[15] M. Ciavarella, C. Murolo, and G. Demelio. *Wear*, 261:1102, 2006.

[16] S. Hyun and M. O. Robbins. *Tribol. Int.*, page doi:10.1016/j.triboint.2007.02.003, in press.

[17] K. L. Johnson. *Contact Mechanics*. Cambridge University Press, Cambridge (1996).

[18] C. Campañá and M. H. Müser. *Europhys. Lett.*, 77:38005, 2007.